



This is an *Accepted Manuscript*, which has been through the RSC Publishing peer review process and has been accepted for publication.

Accepted Manuscripts are published online shortly after acceptance, which is prior to technical editing, formatting and proof reading. This free service from RSC Publishing allows authors to make their results available to the community, in citable form, before publication of the edited article. This *Accepted Manuscript* will be replaced by the edited and formatted *Advance Article* as soon as this is available.

To cite this manuscript please use its permanent Digital Object Identifier (DOI®), which is identical for all formats of publication.

More information about *Accepted Manuscripts* can be found in the [Information for Authors](#).

Please note that technical editing may introduce minor changes to the text and/or graphics contained in the manuscript submitted by the author(s) which may alter content, and that the standard [Terms & Conditions](#) and the [ethical guidelines](#) that apply to the journal are still applicable. In no event shall the RSC be held responsible for any errors or omissions in these *Accepted Manuscript* manuscripts or any consequences arising from the use of any information contained in them.

23 measured for various hybrid nanomaterial arrangements. Both design factors
24 (nanocarbon concentration and network arrangement) influenced the performance of
25 the reduced graphene oxide-based platforms; whereas only nanomaterial arrangement
26 affected the performance of the carbon nanotube-composites. The highest sensitivity
27 towards hydrogen peroxide for reduced graphene oxide nanocomposites (45 ± 3.2
28 $\mu\text{A}/\text{mM}$) was measured for a graphene concentration of $2\text{mg}/\text{mL}$ in a “sandwich”
29 structure; nanoplatinum layers enveloping the reduced graphene oxide. Likewise, the
30 best carbon nanotube performance toward H_2O_2 ($49 \pm 1.4 \mu\text{A}/\text{mM}$) was measured for a
31 sandwich-type structure with nanoplatinum. The enhanced electrocatalytic activity of
32 this “sandwich” structure was due to a combined effect of electrical junctions formed
33 amongst nanocarbon, and nanocomposite soldering to the electrode surface. The top-
34 down carbon/platinum hybrid nanocomposites in this paper represent a simple, low-
35 cost, approach for formation of high fidelity amperometric sensors with remarkable
36 performance characteristics that are similar to bottom-up fabrication approaches.

37

38 **Keywords:** nanocomposite, electrocatalysis, amperometry, biosensor.

39

40 Introduction

41 Carbon and metal nanomaterials have been widely used in the last decade for
42 electroanalytical applications due to their unique electrocatalytic properties, vast surface
43 area-to-volume ratio, robust mechanical strength, and excellent biochemical
44 stability^{1,2,3,4}. Nanomaterials such as reduced graphene oxide, carbon nanotubes, and
45 metal nanoparticles have been extensively used as electrocatalytic platforms in

46 electrochemical biosensors (e.g., amperometric, potentiometric, and impedimetric) to
47 improve sensitivity, response time, and limit of detection. There have been a wide array
48 of graph-from (i.e., bottom-up) and graph-onto (i.e., top-down) synthesis approaches for
49 preparation of carbon/metal hybrid nanocomposites^{5,6}. In general, graph-from
50 approaches are preferred by most labs, although these techniques can be cumbersome
51 and require specialty equipment. Some graph-onto approaches for sensors have
52 demonstrated electron transport rates that are similar to graph-from synthesized
53 sensors^{7,8}.

54 Several studies suggest a synergistic electrocatalytic effect resulting from the
55 conjugation of carbon nanomaterials with metal nanoclusters^{9,10,11,12,13}. Functionalization
56 of reduced graphene oxide or carbon nanotubes with nanometals helps maintain
57 interplanar spacing and can also act as an electrical junction between nanoparticles
58 and/or the electrode surface¹⁴. For instance, Shi et al.¹⁵ reported a microbiosensor
59 platform composed of graphene oxide and amorphous nanoplatinum (i.e., Pt-black).
60 The composite yielded a sensitivity towards hydrogen peroxide of 4.8 $\mu\text{A}/\text{mM}$. The
61 combination of graphene oxide and platinum black was more efficient than either
62 nanomaterial alone in enhancing electron transport. McLamore et al.¹¹ demonstrated
63 the use of platinum black decorated multiwalled carbon nanotubes (MWCNT) as a
64 nanomaterial platform for glucose biosensing. The nanomaterial-mediated micro-
65 biosensor showed sensitivity towards glucose of 531 pA/mM , which was significantly
66 larger than most previously reported glucose micro-biosensors. Tsai & Hong¹³
67 fabricated a Pt–MWCNT–Nafion nanocomposite onto a glassy carbon (GC) electrode
68 for electrochemical oxidation of methanol. The Pt–MWCNT–Nafion platform had higher

69 oxidation of methanol than the Pt-coated GC electrode and the Pt–Nafion-modified
70 electrode. Claussen et al.¹⁶ described two hybrid nanomaterial biosensor platforms,
71 based on networks of single-walled carbon nanotubes conjugated with either palladium
72 nanocubes (Pd nanocube/SWCNT) or platinum nanospheres (Pt nanosphere/SWCNT).
73 These platforms were functionalized with the enzyme glutamate oxidase to create
74 glutamate biosensors. The Pt nanosphere/SWCNT biosensor exhibited significantly
75 enhanced performance compared to previously reported glutamate biosensors, low
76 detection limit (4.6 nM), and a wide linear sensing range (50 nM to 1.6 mM). Claussen
77 et al.¹⁶ suggested that the unique nanoscale- environment of the Pt
78 nanosphere/SWCNT hybrid biosensor could act synergistically to accurately monitor
79 neurotransmitter release/uptake by neurons.

80 Even though enhanced electrocatalysis of metal-nanocarbon composites has
81 been well established, no research efforts have clearly assessed the effect of
82 nanoparticle density and arrangement on electrochemical performance in a detailed
83 comparative study. This study presents common methodologies for developing
84 rapid/low-cost platinum-nanocarbon hybrid nanocomposites for amperometric sensing.
85 The assembly of hybrid nanomaterial platforms based on graphene oxide, multiwalled
86 carbon nanotubes, and nanoplatinum was investigated. The effect of nanocarbon
87 concentration and nanomaterial network arrangement on amperometric performance
88 was studied in detail.

89

90 **Experimental**

91 **Materials and Reagents**

92 Single-layered graphene oxide powder (GO) (height: 0.7-1.2 nm; purity: >99 wt%;
93 manufacturing method: modified Hummers, with no metal catalyst) and multiwall carbon
94 nanotubes powder (MWCNT) (outside diameter: 8-15 nm; purity: 95 wt%; length: 10-50
95 mm; manufacturing method: catalyzed chemical vapor deposition) were purchased from
96 Cheap Tubes Inc (Brattleboro, USA) and used as received. Dimethylformamide (DMF),
97 and lead acetate 30% w/v were obtained from Fisher Scientific (Pittsburgh, USA).
98 Chloroplatinic acid 8 wt.% was procured from Sigma-Aldrich (St. Louis, USA). Hydrogen
99 peroxide 35 wt.%, and potassium nitrate (KNO₃) were acquired from Acros organics
100 (New Jersey, USA). Potassium ferrocyanide trihydrate (K₃Fe(CN)₆) was purchased from
101 EMD chemicals (Billerica, USA). Phosphate buffer saline (PBS) was procured from
102 Mediatech, Inc (Manassas, USA).

103

104 **Hybrid nanomaterial fabrication**

105 Pt/Ir working electrodes (BASI MF-2013, 1.6 mm diameter, 7.5 cm length, 6 mm
106 shaft diameter, CTFE plastic body) were used to test all nanomaterial platforms based
107 on the methods in Shi et al.¹⁷ and McLamore et al.¹¹. Prior to modification, the Pt
108 electrodes were polished with 3, and 1 μm polycrystalline diamond suspensions
109 (Buehler®, USA), rinsed with methanol, and then polished with 0.05 alumina slurry
110 (Buehler®, USA). Finally, electrodes were ultrasonicated in deionized water for 15 min.
111 Amorphous nanoplatinum clusters (nPt) were deposited via electrodeposition in a
112 solution of 0.728% chloroplatinic acid and 0.002% lead acetate. The Pt/Ir electrode was

113 connected to the cathode on a DC power supply (Electro Industries, USA), and a bare
114 platinum wire (0.3 mm diameter; Alfa Aesar, Ward Hill, USA) was connected to the
115 anode. A 10 V constant voltage was applied for 90 seconds based on previously
116 reported methods^{12,15,16}. GO and MWCNT solutions were prepared in DMF to
117 concentrations of 1, 2, and 3 mg/mL. All solutions were ultrasonicated for 15 minutes. 1
118 μ L of the resulting solution was drop-casted on the tip of the Pt/Ir electrodes and dried
119 overnight. GO was reduced during the ultimate electrodeposition of nPt in
120 chloroplatinic acid, which is consistent with Shi et al¹⁵.

121 Eight nanomaterial platform configurations were assembled on the electrode
122 surfaces: Pt/Ir-MWCNT, Pt/Ir-nPt-MWCNT, Pt/Ir-MWCNT-nPt, Pt/Ir-nPt-MWCNT-nPt,
123 and analogously Pt/Ir-GO, Pt/Ir-nPt-GO, Pt/Ir-RGO-nPt, Pt/Ir-nPt-RGO-nPt. Fig. 1
124 shows a schematic of the hybrid nanomaterial configurations. The resulting
125 experimental designs are 3x4 factorials (3 carbon concentrations by 4 nanomaterial
126 configurations) with three observations per cell.

127

128 **Electrochemical Analysis**

129 Electrochemical characterization was performed using a 3 electrode cell stand
130 (C-3, BASi, West Lafayette, IN). Cyclic voltammetry was carried out in 4mM Fe(CN)₆/1M
131 KNO₃ solutions at initial potential of 0 mV and switching potential of 800 mV, versus a
132 Ag/AgCl reference electrode (RE-5B with flexible connector, BASi, West Lafayette, IN)
133 with 10 seconds quiet time, and scan rates of 20, 50, 100, 125, 150, and 200 mV/s. The
134 electroactive surface area of each nanomaterial mediated electrode was determined
135 using the Randles-Sevcik equation¹⁸:

$$i_p = (2.69 \times 10^5) n^{3/2} D^{1/2} C A v^{1/2} \quad (1)$$

136
137 where i_p is the oxidation peak obtained from the cyclic voltammogram, n is the number
138 of transferred electrons in the redox reaction, D is the diffusion coefficient, C is the
139 molar concentration of the working solution, A is the electroactive surface area of the
140 electrode and v is the potential scan rate. Since n , D , and C are known properties of the
141 working solution, A was calculated from the slope of the Cottrell plot (i_p versus $v^{1/2}$).

142

143 DC potential amperometry (DCPA) was conducted in PBS (pH 7.4) at a working
144 potential of +500mV versus Ag/AgCl reference electrode with a sampling rate of 1 kHz.
145 After 5 minutes of polarization, the current output was measured at constant potential
146 while successively injecting hydrogen peroxide (H_2O_2) in the stirred working solution
147 (450 rpm) at 60 second intervals to allow the electrical signal to reach steady state. The
148 dynamic DCPA curves were used to evaluate the performance of the nanomaterial
149 mediated electrodes in terms of sensitivity, response time, and lower limit of detection.

150 Sensitivity was calculated from the slope of the linear portion of the calibration
151 curves. Response time (t_{95}) was obtained by averaging the 95% steady state response
152 time of three successive step changes over the linear range tested (approximately 0-
153 300 μM H_2O_2). The steady state response was determined by performing non-linear
154 regression over single step changes in concentration (exponential rise to maximum/
155 single, 3 parameter/ SigmaPlot 12.0)

156 The lower limit of detection (LOD) was calculated using the 3σ method^{19,20}.

157 **Statistical Analysis**

158 All electrochemical measurements were performed in triplicate. Analysis of
159 variance (ANOVA model I) was performed in order to judge whether or not any effects
160 in electrochemical performance are statistically significant²¹.

161

162 **Imaging and elemental characterization**

163 Morphological characterization of the nanomaterials was conducted via scanning
164 electron microscopy (SEM) and scanning white light interferometry (SWLI). SEM
165 images were taken on a JEOL 5600 LV, with accelerating voltage of 12-15 kV. SWLI
166 profiles (707 μm x 530 μm area) were obtained with a Zygo Newview 7200 with a 20x
167 by 2x objective. A Gauss Spline filter (band-pass mode) with cut-off wavelength of 20
168 μm (low pass) and 0.83 μm (high pass) was applied. Elemental analysis of the
169 nanomaterial platforms were conducted by electron dispersive X-ray spectroscopy
170 (EDS) using an OXFORD INCA 250 operating at 75 kV.

171

172 **Results & Discussion**

173 Fig. 2A shows a representative cyclic voltammogram of a Pt/Ir-nPt-RGO-nPt
174 modified electrode. Each CV in this study exhibited a response characteristic of a
175 reversible couple with well-defined redox peaks, indicating a diffusion controlled
176 reaction at the electrode-solution interface in which the diffusion layer was smaller than
177 the surface area of the electrode. Based on Equation 1, Cottrell plots were prepared to
178 calculate the electroactive surface area of each nanomaterial-modified electrode (a
179 representative plot of a Pt/Ir-nPt-RGO-nPt modified electrode is shown in Fig. 2B).

180 A typical dynamic DCPA curve of a Pt/Ir-nPt-RGO-nPt electrode is displayed in
181 Fig. 3A. Each injection of H_2O_2 produced a current signal which was proportional to the
182 bulk concentration of H_2O_2 in the working solution. Fig. 3B shows a characteristic steady
183 state calibration curve within the linear range of the Pt/Ir-nPt-RGO-nPt electrode. A
184 correlation coefficient (R^2) higher than 0.99 was obtained in each linear regression for
185 the calibration curves of all nanomaterial mediated electrodes. Hydrogen peroxide is the
186 product of several enzyme-catalyzed reactions; oxidative amperometry is the most
187 common type of enzymatic biosensor. Thus, sensor platforms which demonstrate
188 detection of H_2O_2 with high sensitivity and low detection limit are desirable. These
189 nanomaterial composites could serve as platforms for enzymatic biosensors when
190 combined with oxidative enzymes.

191

192 **MWCNT-nPt hybrid nanomaterials**

193 Fig. 4A shows the electroactive surface area of all MWCNT-nPt hybrid electrodes
194 in this study. There were no significant differences in electroactive surface area
195 between the hybrid nanomaterials tested. Both design factors (nanomaterial
196 configuration and MWCNT concentration) had the same effect on the response variable
197 (electroactive surface area) ($p > 0.05$). The highest electroactive surface area was $0.07 \pm$
198 0.015 cm^2 , which was about 3.5 times higher than a bare Pt/Ir electrode.

199 The mean sensitivity towards H_2O_2 for all MWCNT modified electrodes is shown
200 in Fig. 4B. Analysis of variance indicated that only the nanomaterial configuration had a
201 significant effect ($p < 0.05$) on the amperometric sensitivity (see supplemental table 1 for
202 details). Regardless of MWCNT concentration, the highest sensitivity was measured for

203 the Pt/Ir-MWCNT-nPt ($49 \pm 1.4 \mu\text{A}/\text{mM}$) and the Pt/Ir- nPt -MWCNT-nPt (51 ± 15.4
204 $\mu\text{A}/\text{mM}$) platforms. These sensitivity values were approximately 10 times more sensitive
205 than a bare Pt/Ir electrode (See supplemental Figure 1 for representative calibration
206 curves of the MWCNT-based nanomaterial platforms).

207 Hybrid nanocomposites based on carbon nanotubes and metal nanoparticles
208 such as cobalt, gold, palladium, and platinum have been widely used for development of
209 electrochemical devices^{10,13,16,22,23}. These nanocomposites have demonstrated
210 enhanced electrocatalytic properties than either carbon nanotubes, or nanometals
211 alone. Several research groups have suggested that the edge-plane defect sites on the
212 surface of the nanotubes can serve as nucleation sites for the formation of metal
213 nanoclusters. These nanoclusters are thought to establish Ohmic contacts along the
214 nanomaterial network, facilitating formation of high on-state currents^{23,24,25,26}.

215

216 **RGO-nPt hybrid nanomaterials**

217 Fig. 5A shows the average electroactive surface area of the graphene-Pt hybrid
218 nanomaterials. The bare Pt/Ir electrode with GO drop cast on the surface (Pt/Ir-GO) had
219 the lowest electroactive surface area ($0.007 \pm 0.002 \text{ cm}^2$) of all the nanomaterial
220 configurations tested. The Pt/Ir-nPt-GO hybrid had a slightly improved electroactive
221 surface area ($0.033 \pm 0.015 \text{ cm}^2$), although this architecture was not a significant
222 improvement over GO-modified electrodes. The highest electroactive surface area was
223 exhibited by the 2 mg/mL Pt/Ir-nPt-RGO-nPt modified electrode ($0.148 \pm 0.064 \text{ cm}^2$)
224 being at least 7.5 times larger than a bare Pt/Ir electrode ($0.019 \pm 0.003 \text{ cm}^2$).

225 There were significant differences between the mean electroactive surface area
226 for different GO-concentrations within the same nanomaterial configuration. This
227 indicates that the GO-concentration plays an important role on the electrochemical
228 performance of the electrodes. For instance, the Pt/Ir-nPt-GO platform design with GO
229 concentrations of 1 and 2 mg/ml produced cyclic voltammograms similar to those in Fig.
230 2A. However, the 3 mg/ml GO-concentration consistently produced sigmoidal
231 voltammograms, which occur when the diffusion layer thickness is greater than the
232 exposed surface area of the electrode. This indicates that the oxidative current reaches
233 a steady state during the potential scan, impeding the formation of true redox peaks²⁷.

234 The mean sensitivity towards H₂O₂ of all GO-Pt hybrids is presented in Fig. 5B.
235 Similar to the trends from electroactive surface area, the Pt/Ir-GO platform configuration
236 showed the lowest amperometric sensitivity (the average including all GO
237 concentrations was $2.4 \pm 1.2 \mu\text{A}/\text{Mm}$), whereas the 2 mg/mL Pt/Ir-nPt-RGO-nPt
238 modified electrode demonstrated the highest amperometric sensitivity of all the
239 nanomaterial platforms tested ($45 \pm 3.2 \mu\text{A}/\text{mM}$) being about 9 times better than a bare
240 Pt/Ir electrode ($4.9 \pm 0.36 \mu\text{A}/\text{mM}$).

241 Analysis of variance (ANOVA model I) was performed in order to determine
242 whether or not any effects on the response variable (amperometric sensitivity) arising
243 from the GO concentration or the platform configuration were statistically significant. A
244 p-value smaller than the critical value ($p < 0.05$) was obtained for all factors including the
245 interaction between GO concentration and platform configuration, indicating that there is
246 a significant difference in amperometric sensitivity for at least one treatment of each
247 factor (Representative calibration curves of the GO-based nanomaterial platforms are

248 available in supplemental Figure 2). A Tukey test was performed by simultaneously
249 comparing the mean amperometric sensitivity of every factor level to the set of all
250 pairwise comparisons. The four platform configurations were statistically different, and
251 the mean sensitivity obtained using the 2 mg/mL GO concentration was significantly
252 greater than the other concentrations tested. However, there was not a significant
253 difference between the average sensitivities obtained with the 1 and 3 mg/mL GO
254 concentrations (see supplemental data for interaction plots, Anova, and Tukey tables).

255 These results are consistent with other reports describing GO modified
256 electrodes in the literature. Work by Kuila et al.²⁸ demonstrated how oxygen-containing
257 functional groups on the basal planes and edges of GO sheets limit the electrocatalytic
258 capabilities of this nanomaterial. Thus, GO must be reduced to enable the π -electronic
259 conjugation. This explains the low electrocatalytic activity of the Pt/Ir-GO and Pt/Ir-nPt-
260 GO platforms compared to the other two platform designs.

261 The Pt/Ir-RGO-nPt and Pt/Ir-nPt-RGO-nPt hybrid nanomaterials exhibited
262 significantly improved electrochemical performance over all other carbon-metal
263 nanohybrids in this study. Indeed, the electrodeposition of nPt onto GO must have two
264 imperative effects on the electrocatalytic behavior of the platforms: 1) Enhanced
265 electronic π -conjugation due to GO reduction, and 2) Integration of the nanomaterial
266 platform by formation of metal junctions among GO sheets. These nano-junctions
267 electrically connect the carbon-metal nanomaterial network, facilitating electron
268 transport to the surface of the electrode. EDS analysis was used to confirm the partial
269 removal of oxygen functionalities by electrodeposition of Pt nanoparticles on GO. As

270 can be seen in Fig. 6, the atomic percent of oxygen in the Pt/Ir-nPt-RGO-nPt platform
271 (21.4 at%) appears lower than the Pt/Ir-nPt-GO platform (43.2 at%).

272 This result is similar to the study by Wang et al.²⁹. Wang et al. demonstrated
273 efficient reduction of GO during the synthesis of GO/nPt hybrids in chloroplatinic acid.
274 Bonding of Pt nanoparticles onto reduced GO sheets prevents the aggregation of GO
275 and maintains interplanar spacing. In another study, Guo et al.³⁰ reported the synthesis
276 of high quality RGO nanosheets through electrochemical reduction of an exfoliated
277 graphite oxide precursor material at cathodic potentials. Guo et al. concluded that the
278 oxygen-containing functional groups were thoroughly removed from the graphite oxide
279 plane via electrochemical reduction. Using a similar approach, An et al.³¹ described an
280 effective method for the simultaneous electrochemical reduction and electrophoretic
281 deposition of reduced GO on various substrates including Cu, Ni, Al, stainless steel, and
282 p-type Si. An et al found that the electrophoretic deposition process successfully
283 removed the oxygen functional groups in the GO film, improving its electrical
284 conductivity.

285

286 **Comparison of carbon/Pt hybrid nanocomposites**

287 Fig. 7 shows the surface characteristics of the 2 mg/mL carbon/Pt
288 nanocomposites “sandwich” designs using both SWLI and SEM. The morphology of the
289 nPt-CNT hybrid structures are similar to those reported by McLamore et al.¹¹ and Shi et
290 al.¹² (the structures in ref 11 and 12 contained MWCNT directly cast onto electrodes).
291 When compared to the graphene-Pt hybrids, the CNT-nPt nanostructures are
292 heterogenous and have a relatively high degree of aggregation. The average surface

293 roughness coefficient (rms) for the CNT-Pt nanocomposite “sandwich” was 303.3 nm.
294 The surface map for the CNT-Pt nanohybrid shows a rough topography with peaks of
295 irregular height distributed along the plotted area (Fig. 7A). Mono-dispersed deposits of
296 amorphous platinum-black can be seen in the SEM micrograph shown in Fig. 7B. The
297 irregular structure is likely due to poor stacking of MWCNT within the nanohybrid when
298 compared to graphene stacking. The root mean square surface roughness coefficient
299 for reduced graphene-Pt nanohybrids (166.5 nm) was significantly lower than the
300 MWCNT-Pt hybrid sandwich design (Fig. 7C). Together with the enhanced
301 electrocatalytic behavior of RGO relative to MWCNT (Figs. 4 and 5), this indicates that
302 RGO sheets were stacked in a semi-ordered manner between the nPt clusters. SEM
303 images of the RGO-Pt nanohybrid show this smooth stacking and homogenous
304 distribution of nPt along the RGO sheets (Fig. 7D and also EDS data in Fig. 6). The
305 morphology of CNT and graphene structures formed through chemical vapor deposition
306 (CVD) of plasma vapor deposition (PVD) is much more homogenous than the structures
307 formed in these studies^{9,11,16}. Thus, one would expect the performance of CVD or PVD-
308 derived nanocomposites to be far superior to the nanocomposites developed in this
309 study using facile methods. However, when a “sandwich” hybrid nanostructure is
310 created the electron transport is competitive with CVD and PVD formed
311 nanocomposites.

312 Table 1 summarizes the performance characteristics of GO and MWCNT hybrid
313 nanocomposites from this study and similar platforms for amperometric sensors in the
314 literature^{11,32,33,34,35}. As listed in this table, the amperometric sensitivity towards
315 hydrogen peroxide has been greatly improved by the Pt/Ir-MWCNT-nPt and Pt/Ir-nPt-

316 RGO-nPt nanohybrids compared to previous reports. Other performance characteristics
317 (response time, selectivity, limit of detection) for the recipes here are within the range
318 found in the literature. The nanomaterial deposition methodology described in this paper
319 is a simple, fast, and efficient approach for the fabrication of electrocatalytic platforms
320 for amperometric sensors and biosensors. Importantly, the recipe uses commonly
321 available equipment and chemicals, ensuring the methods can be reproduced in any
322 sensor lab. This facile graph-onto methodology is highly efficient and competes with
323 relatively complex graph-from synthesis of carbon-metal hybrid nanocomposites.

324

325 **Conclusions**

326 A facile approach for the fabrication of hybrid nanocomposites based on
327 multiwalled carbon nanotubes, graphene oxide, and nanoplatinum was demonstrated.
328 The effect of carbon concentration and network configuration on electrochemical
329 performance was studied in detail. For the GO-Pt nanohybrids, both design factors
330 played a major role on electrocatalytic response. On the other hand, performance
331 characteristics of the MWCNT nanohybrids were only affected by the configuration
332 factor, and MWCNT concentration in the range of 1 to 3 mg/ml did not have an effect on
333 performance. The network configuration factor affected the electrochemical
334 performance of both GO-based and CNT-based electrodes in a similar manner since in
335 both cases the nanomaterial platforms with nPt on the top layer showed a significantly
336 enhanced amperometric sensitivity compared to the platform configurations with either
337 GO or CNTs on top. This effect was namely attributed to the electrical integration by
338 formation of metal junctions among GO sheets or CNTs. Conversely, the carbon

339 concentration variable in the tested range affected the GO-based and CNT-based
340 electrodes differently. We assume this occurs because the critical concentration of
341 these two materials is inherently different. In the GO case, a low carbon concentration
342 (e.g. 1 mg/mL) resulted in isolated sheets deposited in random orientations leading to a
343 poor electronic conjugation to the electrode's surface; in the other hand, a large
344 concentration (e.g. 3 mg/mL) resulted in stacking of GO sheets turning them into
345 graphitic structures with lower electrical conductivity. Thus, there was a middle point
346 where enhanced electrochemical performance was achieved (e.g. 2 mg/mL). We
347 believe that a similar effect (with an optimal carbon concentration) could be observed
348 with CNTs, but perhaps in a wider concentration range.

349 Some of the reduced GO and MWCNT-nanocomposite platforms show promising
350 potential for the development of highly sensitive amperometric biosensors. Future
351 enhancements to the GO-based platforms may include further removal of oxygen
352 functional groups by a low-cost/environmentally-friendly reducing agent such as
353 magnesium chloride or ascorbic acid.

354

355 **Acknowledgements**

356 The authors would like to thank the Colombian funding agencies Colfuturo and
357 Colciencias, the Agricultural and Biological Engineering Department of the University of
358 Florida, the FAMU Feeder Program, and the UF Early Career Award for the financial
359 support.

360

361 **References**

- 362 1 A. Chen and S. Chatterjee, *Chem. Soc. Rev.*, 2013, 42(12), 5425–38.
- 363 2 J.J. Gooding, *Electrochim. Acta*, 2005, 50(15), 3049–3060.
- 364 3 D. Hernandez-Santos, M.B. Gonzalez-Garcia and A. Costa-Garcia,
365 *Electroanalysis*, 2002, 14(18), 1225–1235.
- 366 4 Y. Shao, J. Wang, H. Wu, J. Liu, I.A. Aksay and Y. Lin, *Electroanalysis*, 2010,
367 22(10), 1027–1036.
- 368 5 A. K. Geim and K. S. Novoselov, *Nat. Mater.*, 2007, 6, 183–91.
- 369 6 Z.J. Fan, J. Yan, T. Wei, G.Q. Ning, L.J. Zhi, J.C. Liu, D.X. Cao, G.L. Wang and
370 F. Wei, *ACS Nano*, 2011, 5, 2787–2794.
- 371 7 S. Stankovich, D. a Dikin, G. H. B. Dommett, K. M. Kohlhaas, E. J. Zimney, E. a
372 Stach, R. D. Piner, S. T. Nguyen, and R. S. Ruoff, *Nature*, 2006, 442, 282–6.
- 373 8 R. Muszynski, B. Seger, and P. V. Kamat, *J. Phys. Chem. C*, 2008, 112, 5263–
374 5266.
- 375 9 J.C. Claussen, S.S. Kim, A.U. Haque, M.S. Artilles, D.M. Porterfield and T.S.
376 Fisher, *Journal of diabetes science and technology*, 2010, 4(2), 312–9.
- 377 10 L. Han, Q. Wang, S. Tricard, J. Liu, J. Fang, J. Zhao and W. Shen, *RSC Adv.*,
378 2013, 3(1), 281.
- 379 11 E.S. McLamore, J. Shi, D. Jaroch, J.C. Claussen, A. Uchida, Y. Jiang, W. Zhang,
380 S.S. Donkin, M.K. Banks, K.K. Buhman, D. Teegarden, J.L. Rickus and D.M.
381 Porterfield, *Biosens. Bioelectron.*, 2011, 26(5), 2237–45.
- 382 12 J. Shi, E.S. McLamore and D.M. Porterfield, *Biosens Bioelectron.*, 2013, 40(1),
383 127–34.

- 384 13 Y.C. Tsai and Y.H. Hong, *J. Solid State Electrochem.*, 2008, 12(10), 1293–1299.
- 385 14 B.L. Huang and C.Y. Mou, *EPL (Europhysics Letters)*, 2009, 88(6), 68005.
- 386 15 J. Shi, H. Zhang, A. Snyder, M. Wang, J. Xie, D.M. Porterfield and L.A. Stanciu,
387 *Biosens. Bioelectron.*, 2012, 38(1), 314–320.
- 388 16 J.C. Claussen, M.S. Artilés, E.S. McLamore, S. Mohanty, J. Shi, J.L. Rickus, T.S.
389 Fisher and D.M. Porterfield, *J. Mater. Chem.*, 2011, 21(30), 11224.
- 390 17 J. Shi, J.C. Claussen, E.S. McLamore, A. ul Haque, D. Jaroch, A.R. Diggs, P.
391 Calvo-Marzal, J.L. Rickus and D.M. Porterfield, *Nanotechnology*, 2011, 22(35),
392 355502.
- 393 18 J. Wang, *Analytical electrochemistry*, John Wiley & Sons, Inc. New York, 3rd edn.,
394 2006.
- 395 19 IUPAC Compendium of Chemical Terminology, 2012, *In IUPAC Gold Book*, p.
396 3540. doi:10.1351/goldbook.L03540
- 397 20 D. Diamond, *Principles of Chemical and Biological Sensors*, ed. J.D.
398 Winefordner, John Wiley & Sons, Inc. New York, 1st edn., 1998, vol. 150.
- 399 21 L. Ott, *An introduction to statistical methos and data analysis*, Wadsworth, Inc.,
400 Belmont, Ca, 4th edn., 1993.
- 401 22 X. Chu, D. Duan, G. Shen and R. Yu, *Talanta*, 2007, 71(5), 2040–7.
- 402 23 J. Wang, S. Yang, D. Guo, P. Yu, D. Li, J. Ye and L. Mao, *Electrochem.*
403 *Commun.*, 2009, 11(10), 1892–1895.
- 404 24 S. Ilani and P.L. McEuen, *Annu. Rev. Condens. Matter Phys.*, 2010, 1(1), 1–25.
- 405 25 A.B. Kaiser and V. Skákalová, *Chem. Soc. Rev.*, 2011, 40(7), 3786–801.
- 406 26 J. Svensson and E.E.B. Campbell, *J. Appl. Phys*, 2011, 110(111101), 1–16.

- 407 27 A.J. Bard and L.R. Faulkner, *Electrochemical methods: fundamentals and*
408 *applications*, John Wiley & Sons, Inc., New York, 2nd edn., 2001.
- 409 28 T. Kuila, A.K. Mishra, P. Khanra, N.H. Kim and J.H. Lee, *Nanoscale*, 2013, 5(1),
410 52–71.
- 411 29 Y. Wang, J. Liu, L. Liu and D.D. Sun, *Nanoscale Res. Lett.*, 2011, 6(1), 241.
- 412 30 H.L. Guo, X.F. Wang, Q.Y. Qian, F.B. Wang and X.H. Xia, *ACS nano*, 2009, 3(9),
413 2653–9.
- 414 31 S.J. An, Y. Zhu, S.H. Lee, M.D. Stoller, T. Emilsson, S. Park, A. Velamakanni, J.
415 An and R.S. Ruoff, *J. Phys. Chem. Lett.*, 2010, 1(8), 1259–1263.
- 416 32 S. Woo, Y.R. Kim, T.D. Chung, Y. Piao and H. Kim, *Electrochim. Acta*, 2012, 59,
417 509–514.
- 418 33 X. Dong, Y. Ma, G. Zhu, Y. Huang, J. Wang, M.B. Chan-Park, L. Wang, W.
419 Huang and P. Chen, *J. Mater. Chem.*, 2012, 22(33), 17044.
- 420 34 Y. Fang, S. Guo, C. Zhu, Y. Zhai and E. Wang, *Langmuir: the ACS journal of*
421 *surfaces and colloids*, 2010, 26(13), 11277–82.
- 422 35 S. Chakraborty and C.R. Raj, *Biosens. Bioelectron.*, 2009, 24(11), 3264–8.
423

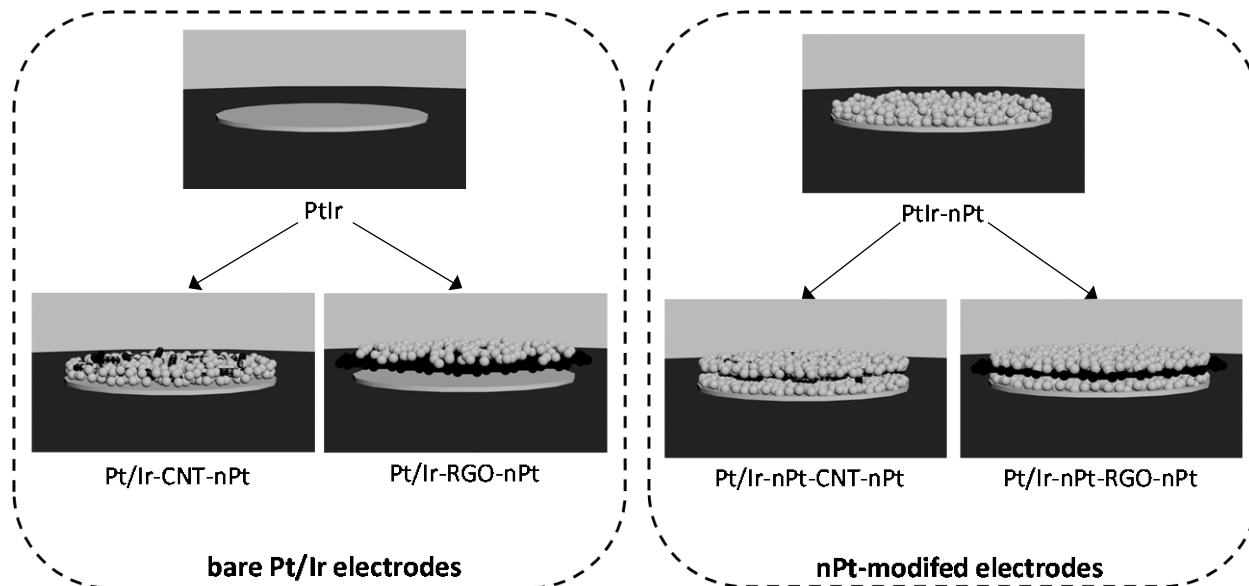
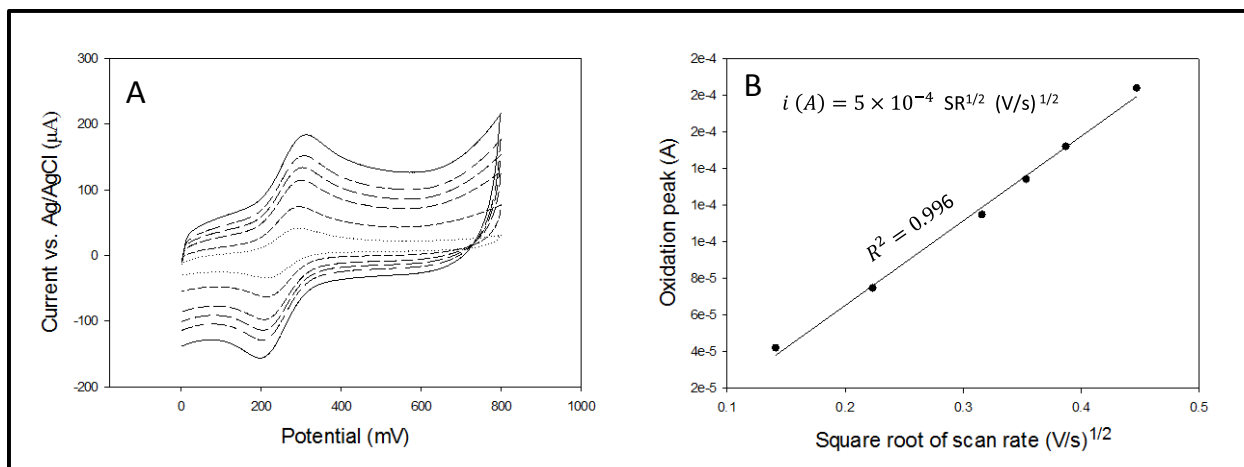
424 **Figures**

Fig. 1 Schematic representation of nanomaterial platforms assembled on platinum/iridium (Pt/Ir) electrodes: (left) carbon nanotubes (CNT) or reduced graphene oxide sheets (RGO) were first deposited at concentrations of 1,2, and 3 mg/mL, followed by electrodeposition of nanoplatinum clusters (nPt). (right) A nPt-nanocarbon-nPt “sandwich” was formed at nanocarbon concentrations of 1,2, and 3 mg/mL.



433

434 **Fig. 2** A) Representative cyclic voltammograms of a Pt/Ir-nPt-RGO-nPt modified435 electrode in 4mM Fe(CN)₆/1M KNO₃ solution at different voltage scan rates. The

436 magnitude of the electrical signal increases as the scan-rate increases. B)

437 Characteristic Cottrell plot of a Pt/Ir-nPt-RGO-nPt modified electrode. The calculated

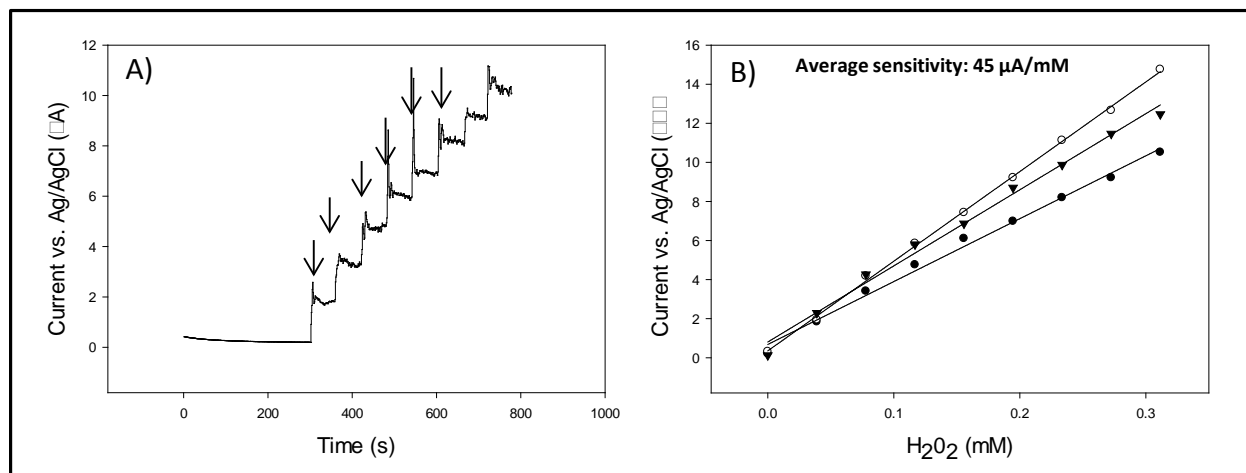
438 electroactive surface area was 0.18 cm².

439

440

441

442



443

444 **Fig. 3** A) Representative DCPA curve showing the current response to successive
445 injections of hydrogen peroxide (injection times are indicated by vertical arrows). B)
446 Characteristic calibration curves for the sensor. Each treatment was tested by
447 triplicates.

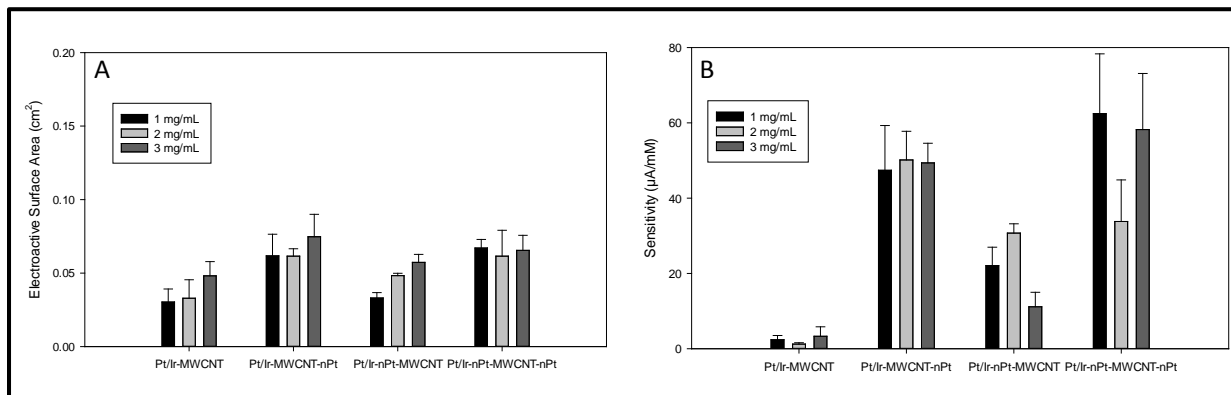
448

449

450

451

452



453

454 **Fig. 4** Electrochemical performance of the MWCNT-based nanomaterial platforms. A)

455 Comparison between electroactive surface areas. B) Comparison between sensitivities.

456 Error bars denote the standard error of the arithmetic mean of the measurements (n=3).

457 Inset boxes indicate the concentration of MWCNT (panel A) or GO (panel B) used in

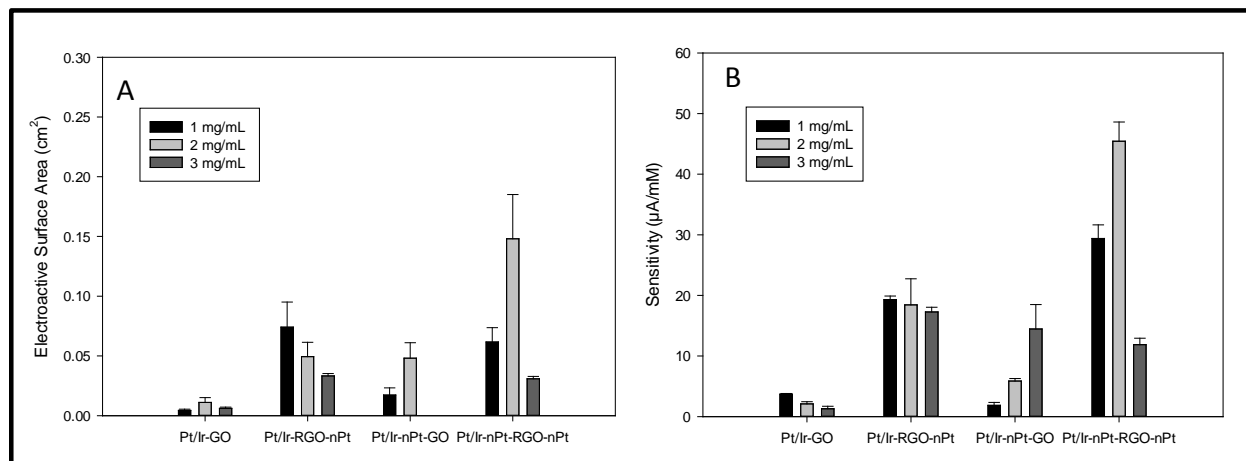
458 combination with each nanomaterial configuration.

459

460

461

462



463

464 **Fig. 5** Electrochemical performance of the GO-based nanomaterial platforms. A)
465 Comparison between electroactive surface areas. B) Comparison between sensitivities.
466 Error bars denote the standard error of the arithmetic mean of the measurements (n=3).

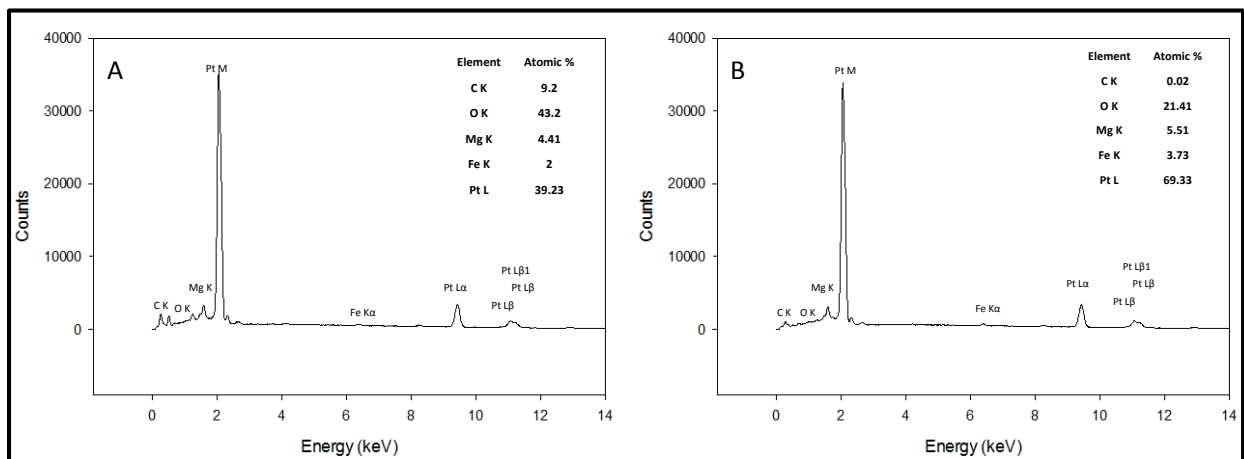
467 Inset boxes indicate the concentration of MWCNT (panel A) or GO (panel B) used in
468 combination with each nanomaterial configuration.

469

470

471

472



473

474 **Fig. 6** A) EDS spectrum of the 2 mg/ml Pt/Ir-nPt-GO nanomaterial platform. B) EDS

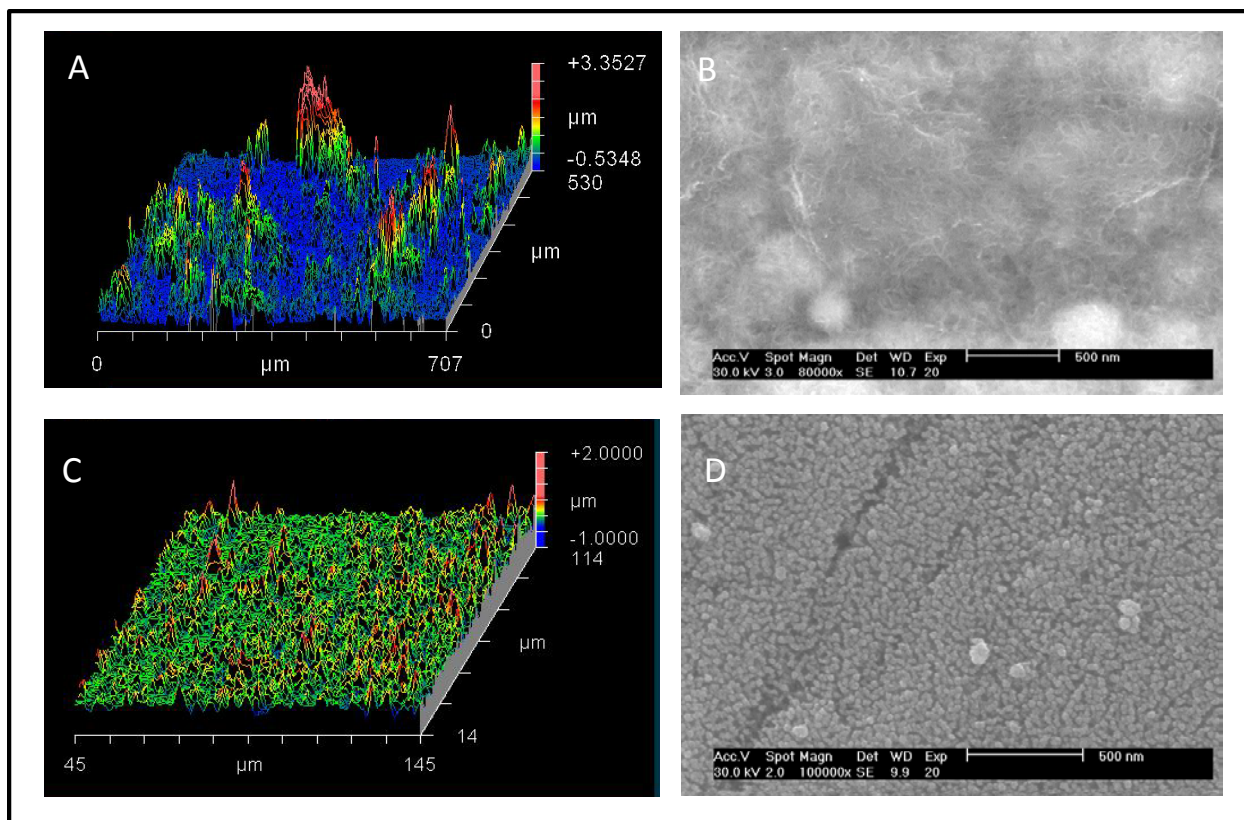
475 spectrum of the 2 mg/ml Pt/Ir-nPt-GO-nPt nanomaterial platform.

476

477

478

479



480

481 **Fig. 7** Surface topography of 2 mg/mL CNT-Pt and graphene-Pt nanocomposites
482 “sandwich” hybrids. A) SWLI surface map of 707 X 530 μm area for MWCNT-Pt
483 nanohybrid sandwich. B) Representative SEM micrograph of MWCTN-Pt sandwich
484 surface. C) SWLI surface map of graphene-Pt hybrid for a 100 X 100 μm area. D)
485 Representative SEM micrograph of surface for RGO-Pt sandwich.

486

487

488

489

490 **Tables**

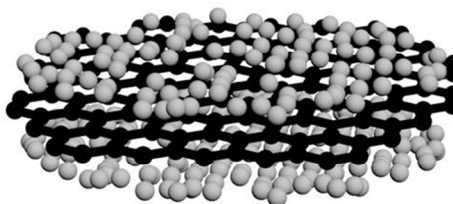
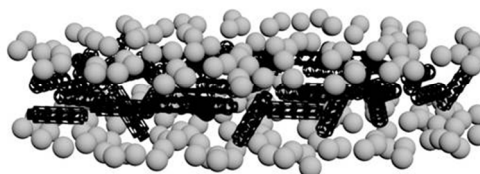
491 **Table 1.** Summary of some recent nanomaterial platform designs for amperometric
 492 sensors

Platform	Sensitivity ($\mu\text{A}/\text{mM}$)	Response time (s)	LOD (μM)	Reference
Pt/Ir-nPt-GO-nPt	$45 \pm 7\%$	$3 \pm 22\%$	$0.14 \pm 28\%$	This work
Pt/Ir-MWCNT-nPt	$49 \pm 15\%$	$3 \pm 14\%$	$0.43 \pm 32\%$	This work
Graphene/MWCNTs	$2.1 \pm \text{NR}$	NR	$9.4 \pm 2.8\%$	Woo et al. ³²
Graphene/CNT	$15 \pm \text{NR}$	NR	$1 \pm \text{NR}$	Dong et al. ³³
Graphene/AuNP	NR	$5 \pm \text{NR}$	$0.22 \pm \text{NR}$	Fang et al. ³⁴
GrOx/Pt black	$4.8 \pm 46\%$	NR	NR	Shi et al. ¹¹
Nano-Pt	$9.15 \pm \text{NR}$	NR	$5 \times 10^{-4} \pm \text{NR}$	Chakraborty & Raj ³⁵

493 *NR=Not reported in manuscript*

494

Table of contents entry

Nanohybrid sandwichGraphene-
nanoplatinum hybridCNT-nanoplatinum
hybrid

This facile graph-onto methodology is highly efficient and competes with relatively complex graph-from synthesis of carbon-metal hybrid nanocomposites.